5-2008

Micro Air Vehicle (MAV): Numerical Optimization of a Coaxial Rotor Blade Design

Jeffrey A. Kornuta

Micro Air Vehicle (MAV): Numerical Optimization of a Coaxial Rotor Blade Design

by

Jeffrey A. Kornuta

Undergraduate honors thesis under the direction of

Dr. Shengmin Guo

Department of Mechanical Engineering

Submitted to the LSU Honors College in partial fulfillment of
the Upper Division Honors Program.

May 2008

Louisiana State University
& Agricultural and Mechanical College
Baton Rouge, Louisiana

Abstract

A micro air vehicle (MAV) is defined as a remotely operated aircraft with a maximum linear dimension of approximately six inches. The objective of this project is to design and manufacture a MAV with surveillance capabilities that can maintain stable, controlled flight. Applications for such a vehicle are numerous, especially for deployment in potentially hostile environments where human life would be at risk. This paper describes the requirements and design of a micro coaxial helicopter, specifically focusing on the numerical optimization of the rotor blades using an extenstion of Prandtl's lifting-line theory. After performing the numerical optimization, an ideal rotor blade geometry would possess an Althaus 7-476 airfoil profile, a linear taper ratio of 0.3, and a linear twist variation of $18^\circ \rightarrow 15^\circ$ from root to tip.

Nomenclature

Γ	Circulation
y	Blade coordinate axis
α_i	Induced angle of attack
w	Downwash velocity
y_0	Particular y-location on blade
r	Blade coordinate axis
R	Total length of blade
b	Blade length under analysis
x	Blade fraction omitted from analysis
Ω	Rotational speed of blade, rad/s
U	Blade freestream velocity
t_c	Thrust coefficient
T	Thrust
ρ	Air density
A	Rotor disc area
s	Rotor solidity
n	Number of rotor blades
c	Chord length
z^*	Dimensionless blade coordinate axis
q_c	Torque coefficient
Q	Torque
δ	Dimensionless torque parameter
c_l	Section lift coefficient
α_{eff}	Effective angle of attack
M	Figure of merit
$\hat{\Omega}$	Blade speed required for hover, rev/min
W	Weight of MAV, newtons
N	Even number of computational nodes
$\mathbb{N}$	Set of natural numbers
Γ_0	Initial Γ profile parameter
Δy	Distance between computational nodes
F_i	Integrand shorthand
α	Blade pitch
Γ'	New circulation
d	Convergence parameter
D	Convergence damping parameter
Δz^*	Dimensionless distance between nodes
δ_{avg}	Average dimensionless torque parameter
B	Thrust coefficient correction factor
a	Taper ratio
c_t	Chord at blade tip
c_r	Chord at blade root
c_{avg}	Average chord length
$\mathbf{c}$	Tip/root chord vector
L'	Lift per unit span, N/m^2
α_0	Initial pitch at blade root

Subscript

j	j-th node (odd)
k	k-th node (even)

Contents

List of Figures

1 Introduction

MICRO air vehicles (MAVs) are commonly described as remote controlled flying vehicles with no linear dimension exceeding six inches (15.24 cm) [8]. Ideally, a MAV would be designed to carry a usable payload that could be deployed in potentially hostile environments while the operator remains at a safe distance. Usable payloads would include sensors to detect biological, chemical, or radiological hazards, as well as cameras to transmit real time images of distant objects to the operator.

Various competitions are held worldwide to encourage innovation in the design and manufacturing of MAVs [1]. These competitions typically have surveillance events where targets obscured from ground level observation are visually identified and photographed by the MAV controllers. Competitions such as these help spur creativity among enthusiasts and benefit the scientific community by introducing novel ideas and prototypes that can further the development of future micro air vehicles.

Figure 1: MAV being tested by the US Navy in China Lake, CA [11].

1.1 Motivation

Motivation for this particular project stems from a general interest in aerospace topics among the design team members[1]. Additionally, the apparent complexity and difficulty of the project serves as a worthwhile and challenging goal that each team member would like to contribute towards. To the teams' knowledge, no LSU team has been able to successfully

[1]Team members for the MAV project include mechanical engineering undergraduates Diane Ho, Jeffrey Kornuta, Lauren Peltier, and Richie Sajan.

construct a functional MAV, despite their hard efforts. Thus, designing and building a working prototype would not only serve as a good engineering exercise, but the process would ultimately instill personal satisfaction in each of the students on the MAV team. Also, by actively participating in this project, the team members will not only learn concepts vital to aircraft and electronics design, but they will also acquire several skills that will prepare them for the aerospace workforce. These skills encompass teamwork, project management, and an aptitude for effective communication through both written and oral presentations. By becoming adept in these areas, team members will be able to make a smooth transition from higher education to the workforce; thus, this project will successfully prepare the student team for future work in the aerospace industry.

1.2 Objectives

The primary objective of this project is to design and manufacture a micro air vehicle with surveillance capabilities that can maintain stable, controlled flight. Accordingly, this MAV must be able to fulfill certain tasks in order to be considered a successful surveillance tool; these tasks are defined as follows:

- The MAV must be able to obtain an adequate real-time video feed during the course of the flight, as well as remotely transmit this feed up to 200 meters away from the operator (line-of-sight). Indoor flights have no transmission distance requirements, given the varied geometrical and material parameters of different buildings.
- The longest edge of the MAV must remain approximately within the size constrains of a standard MAV (6–8 inches). To be specific, the MAV must fit inside a 7 in $\times$ 7 in $\times$ 7 in box.
- The MAV must be able to fly for approximately ten minutes in indoor and outdoor environments; however, outdoor flights are limited to light winds, no precipitation, and daytime conditions.
- The operator must be able to fully control the MAV on all x-y-z axes, as well as be able adjust the control settings for maximum stability.
- The final MAV must cost less than \$650 by itself and less than \$1200 with the required video equipment.

By meeting these specific objectives, this MAV would be a valuable surveillance tool for many applications, including various industrial, governmental, and military projects.

1.3 Subsystem Breakdown

The proposed solution to the project utilizes a helicopter-type design in order to accomplish the specified objectives. This type of design has several advantages over a fixed wing design:

- Does not require manual launching

- Has excellent maneuverability
- Capable of remaining stationary for superb observation
- Improved aerodynamic properties as compared to fixed wing MAVs

In addition to being helicopter based, the MAV will utilize two counter-rotating (coaxial) blades in order to produce lift and maintain stability, as opposed to a typical helicopter design, which uses one main rotor and one tail rotor to operate. As a result, the overall size of the craft can be minimized, and the extra rotor allows the rotor blade system to move more air, thus enhancing the overall stability of the MAV. Additionally, small scale coaxial helicopters have been found to produce better efficiencies than single-rotor helicopters during hover [3].

Each of the main rotors will be powered by a separate brushless DC electric motor connected to an array of 2-cell lithium-polymer batteries. By adjusting the relative speeds of each of the rotor blades, the yaw of the fuselage can be adjusted to any orientation. Also, by utilizing adjustable swash plates, the pitch and roll of the aircraft can be controlled with a fairly minimum complexity [Figure 2].

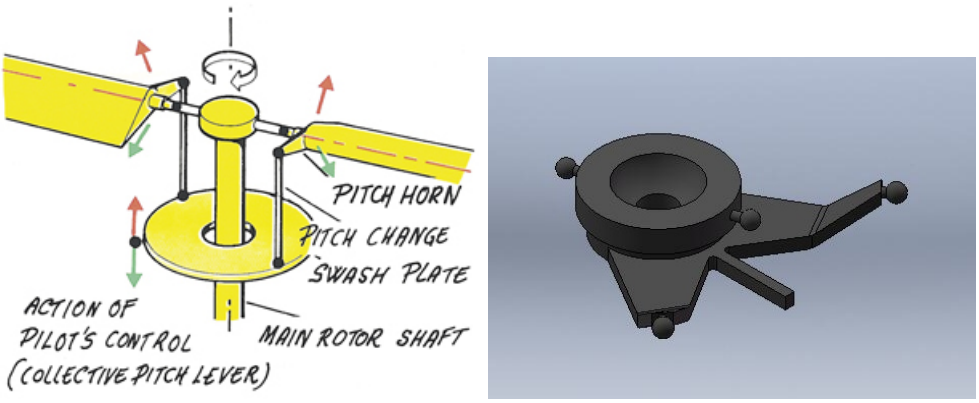

Figure 2: (a) Diagram of a typical helicopter swash plate [10]; (b) CAD model of the swash plate used on the MAV.

The electronics within the MAV would consist of several components within two main categories: surveillance and control. Surveillance electronics consist of a miniature video camera, a wireless transmitter, and an adequate antenna. The miniature CCD video camera will deliver a live video feed wirelessly via a 2.4 GHz transmitter to a receiver unit connected to a laptop computer that records the feed. Utilizing a camera with an approximate weight of 20 grams and a resolution of 250k pixels, the vehicle will be able to adequately monitor its surroundings with minimal stress on the power system. Moreover, the MAV can be flown by line of sight or by on-board camera, allowing for great flexibility in the method by which the craft is flown.

The control electronics consist of two swash plate servos, two electronic speed controllers (ESCs), and a solid state (heading hold) gyroscope [Figure 3]. The ESCs, which control

each of the main rotors, mainly determine the collective position of the MAV, controlling the upward and downward position of the vehicle. The swash plate servos, as mentioned previously, control the position of the swash plate, adjusting the roll and pitch of the aircraft. The electronic heading hold gyroscope automatically holds the yaw of the aircraft in a fixed position, yet it can also adjust the yaw via signals sent from the operator. Thus, the MAV operator is able to control the orientation of the aircraft with greater ease, allowing for a greater operation reliability.

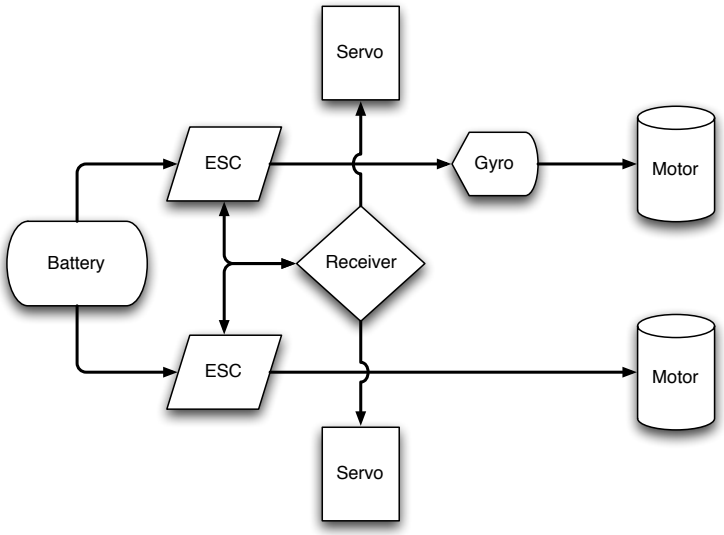

Figure 3: MAV control system flow diagram.

Additionally, one of the most important considerations made in the final prototype design is the optimization of the rotor blade geometry. In order for to meet (or exceed) the flight time objectives that were defined previously, the DC motors must exert as little a load as possible on the power system. This goal of power minimization can be achieved predominantly by designing optimized rotor blades that maximize lift while minimizing their required speed for hover. By carefully studying fundamental aerodynamic theories, producing a detailed mathematical model, and implementing proper numerical techniques, an optimized rotor blade can certainly be designed. The next section introduces and explains the methods used in designing the rotor blade geometry.

2 Aerodynamics

2.1 Background & Theory

2.1.1 Airfoils

In order to understand the analysis behind the design of the rotor blades, one must first grasp the underlying principles behind airfoils. An aifoil is defined as a two-dimensional construct

whose purpose is to produce aerodynamic lift. Below is a diagram explaining common airfoil nomenclature [Figure 4].

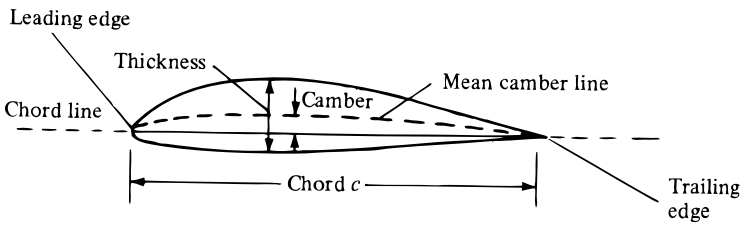

Figure 4: Common airfoil nomenclature [2].

To produce lift, airfoils must either have a nonzero camber or be positioned at a positive angle of attack. In this way, the flow of air around the airfoil produces a lower pressure on the upper surface, creating a lift-inducing pressure differential between the upper and lower surfaces. The zero-lift angle of attack $\alpha_{L=0}$ indicates whether or not an airfoil has camber: $\alpha_{L=0} = 0$ corresponds to a symmetric airfoil while $\alpha_{L=0} < 0$ corresponds to a cambered airfoil [Figure 5].

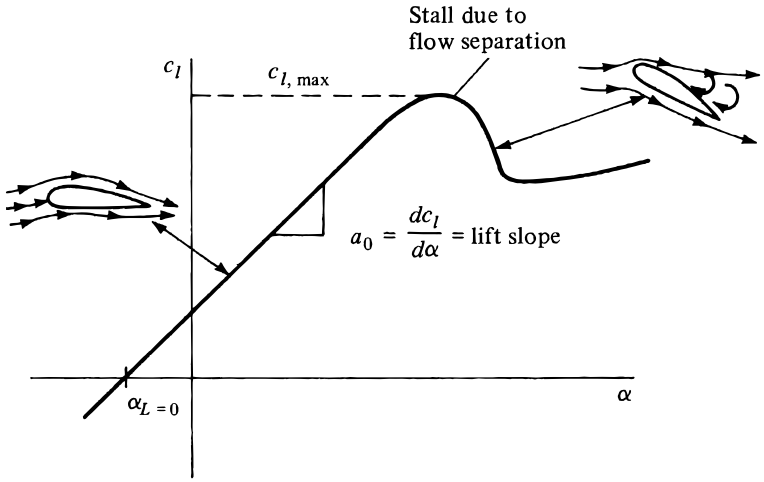

Figure 5: Example graph of $c_l(\alpha)$ [2].

For most cases, the lift slope[2] $dc_l/d\alpha$ is a constant approximately equal to 2π, provided that the airfoil is thin [2]. However, depending on the value of the Reynolds Number[3], $c_l(\alpha)$ reaches a maximum at $dc_l(\alpha)/d\alpha = 0$ at a particular angle of attack. At this critical α, which is known as the stall angle, the airfoil is said to be stalled with a maximum lift coefficient $c_{l,\max}$. This maximum occurs as a result of flow separation induced by the viscous effects of air.

[2]The lift coefficient $c_l \equiv L'/q_\infty c$, where L' is the lift per unit span, $q_\infty \equiv \frac{1}{2}\rho_\infty V_\infty^2$, and c is the chord length.

[3]$\mathrm{Re} \equiv \rho_\infty V_\infty c/\mu_\infty$, where ρ and μ are the density and dynamic viscosity of the fluid, V_∞ is the freestream velocity, and c is the characteristic (chord) length.

2.1.2 Downwash: A Result of Finite Wings

Though airfoil theory offers good insight into the problem of rotor blade optimization, further investigation is necessary. No practical aircraft utilizes an airfoil by itself; instead, most aircraft employ wings, a three-dimensional construct of finite span. Since b does not extend to $\pm\infty$ [Figure 6], the lift distribution over the span is not constant. This phenomenon is due to the presence of tip effects, which merely describes how the air below a wing tends to flow towards the upper surface of a wing around the wing tips due to a substantial pressure difference between the upper and lower surfaces. As one can imagine, these tip effects increase as the amount of lift increases, and they also result in wing-tip vortices that trail the wing [Figure 7].

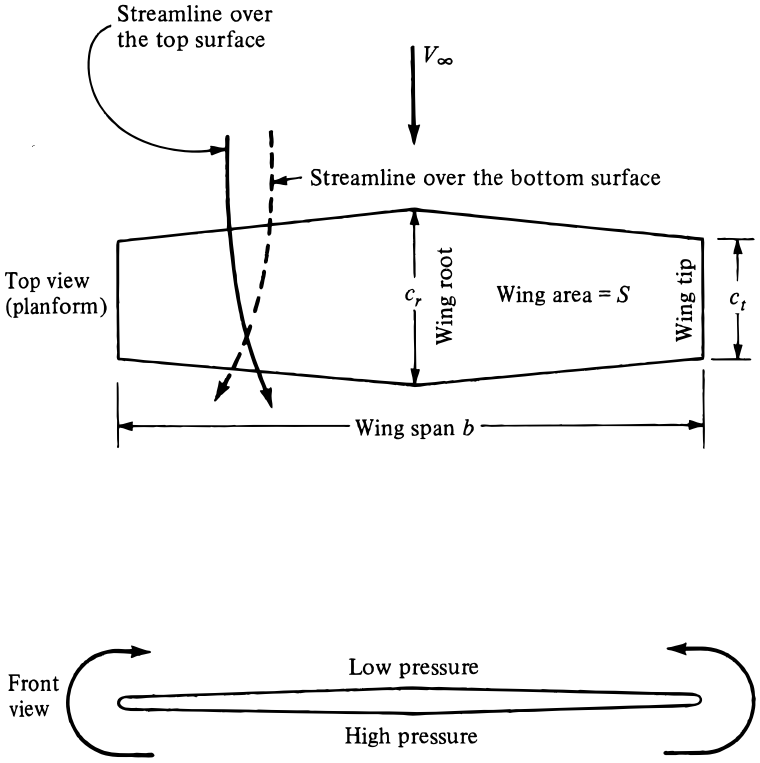

Figure 6: Diagram of a finite dimensional wing [2].

However amazing they may be, wing-tip effects actually decrease the amount of lift a wing may produce when compared to an equivalent airfoil; in fact, they even produce a drag component. This component of drag is due to the downwash velocity w caused by these tip effects [Figure 8]. As a result, this downwash slightly adjusts the direction of the freestream velocity that the wing "sees"; moreover, an induced angle of attack can be defined between this local relative wind and V_∞. The induced angle of attack α_i is important because the overall lift per unit span of a certain wing section can be found using a modified angle of attack—the difference between α and α_i. This angle of attack is known as the effective angle of attack $\alpha_{\text{eff}} = \alpha - \alpha_i$.

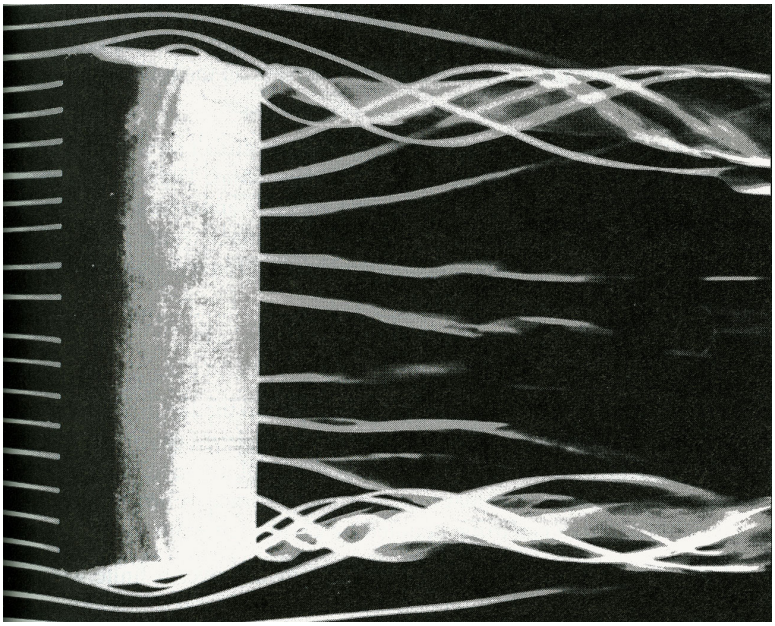

Figure 7: Photograph of wing-tip vortices [2].

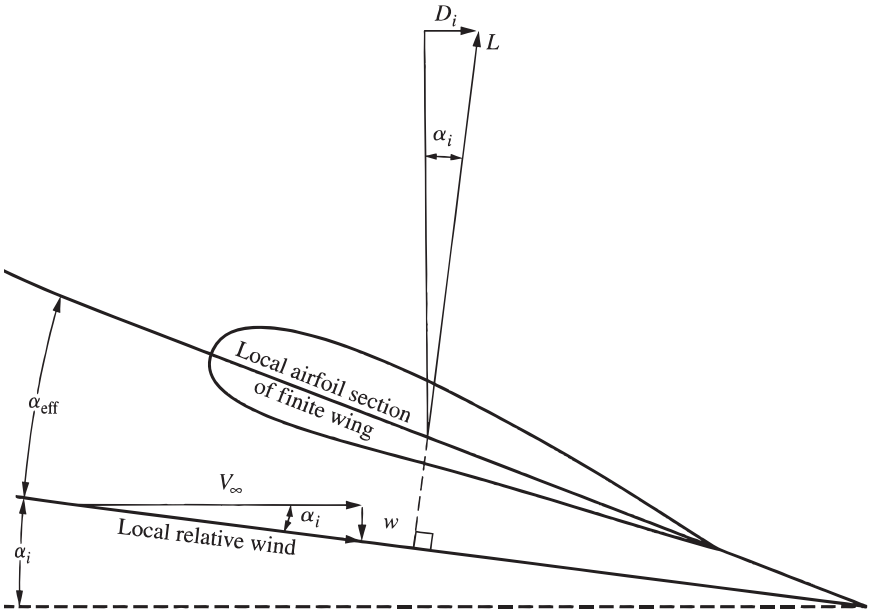

Figure 8: An airfoil section with induced characteristics due to tip effects [2].

2.1.3 Vortex Filaments & the Biot-Savart Law

In order to determine how to find the downwash velocity w and the corresponding induced angle of attack α_i, several other aerodynamic concepts must be introduced. Assume that a two-dimensional point vortex of strength Γ is extended outward (in and out of the page) to $\pm\infty$ with a positively-defined clockwise flow. Such an object is termed a vortex filament. As with a point vortex, the induced velocity at a point orthogonal to the filament varies inversely with the distance from the center of the vortex, and the magnitude of the velocity is equal to the magnitude of the velocity in the direction tangential to the filament. However, if the filament is curved, the velocity at some arbitrary point P must be described differently.

Recall the Biot-Savart law that describes the magnetic field strength from electromagnetic theory [7]:

$$d\mathbf{B} = \frac{\mu I}{4\pi}\frac{d\mathbf{l}\times\mathbf{r}}{|\mathbf{r}|^3},$$

where $d\mathbf{B}$ is the induced magnetic field strength induced at some point P by a differential segment of wire $d\mathbf{l}$ pointing in the direction of its electrical current I. Also, $\mathbf{r}$ is the vector pointing from $d\mathbf{l}$ to point P, while μ is the permeability of the medium surrounding the wire.

This equation is directly analogous to the induced velocity at an arbitrary point due to a vortex filament. In fact, the Biot-Savart law in inviscid, incompressible flow theory is described as follows:

$$d\mathbf{V} = \frac{\Gamma}{4\pi}\frac{d\mathbf{l}\times\mathbf{r}}{|\mathbf{r}|^3}, \tag{1}$$

where $d\mathbf{V}$ is the induced velocity at some point P due to a differential segment $d\mathbf{l}$ of a vortex filament of strength Γ [Figure 9]. When this general case is applied to a straight vortex filament, the induced velocity at a point P reduces to the familiar result

$$V = \frac{\Gamma}{2\pi h}, \tag{2}$$

where h is the perpendicular distance from the filament to P.

2.1.4 Prandtl's Lifting-Line Theory

According to Helmholtz's vortex theorems [2],

1. the strength of a vortex filament is constant along its length, and
2. a vortex filament cannot end in a fluid; thus, it must extend infinitely or form a closed path.

Given this information, let us transform a finite wing into a single vortex filament shaped like a horseshoe [Figure 10]. This transformation makes sense because of the Kutta-Joukowski theorem

$$L' = \rho_\infty V_\infty \Gamma, \tag{3}$$

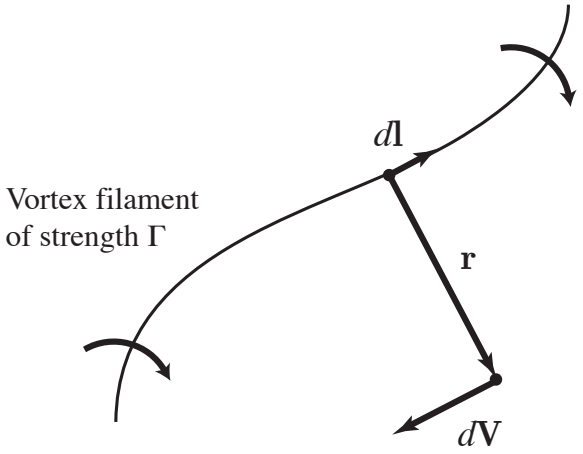

Figure 9: General case of a vortex filament: the Biot-Savart law.

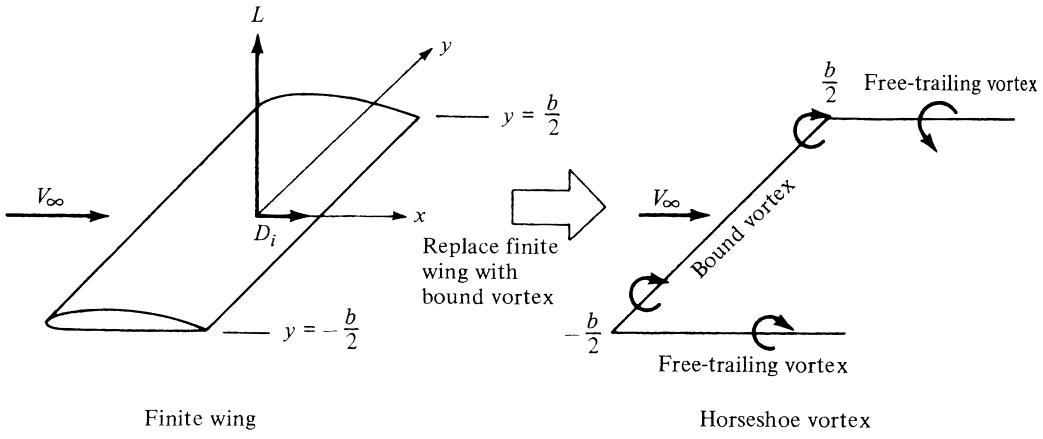

Figure 10: Replacement of a wing with a horseshoe vortex [2].

which states that the lift per unit span is equal to the product of the freestream density, freestream velocity, and the circulation. In this case, the strength of the vortex filament represents the circulation around the wing [Figure 11]. Circulation is defined as follows:

$$\Gamma \equiv -\oint_A \mathbf{V} \cdot d\mathbf{s} = -\iint_S (\nabla \times \mathbf{V}) \cdot \hat{\mathbf{n}}\, dS. \tag{4}$$

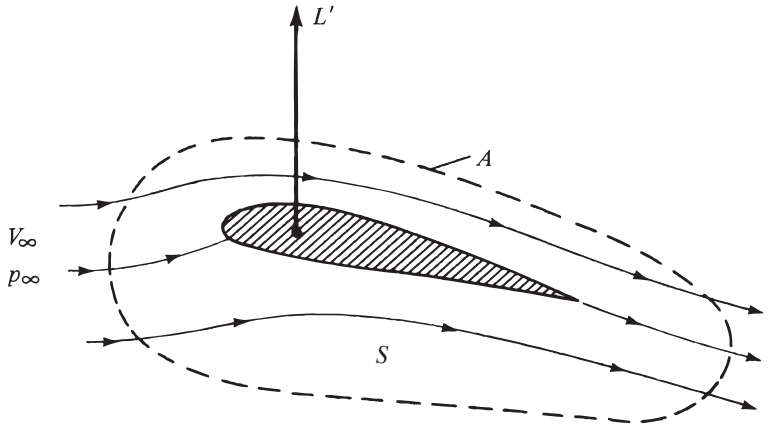

Figure 11: Circulation around an airfoil section [2].

Using Eq.2, the downwash velocity can be expressed as

$$w(y) = -\frac{\Gamma}{4\pi} \frac{b}{(b/2)^2 - y^2}. \tag{5}$$

Though this equation may seem sufficient to express $w(y)$, we find that the downwash velocity becomes extremely large near the wing tips. In fact,

$$\lim_{y \to \pm b/2} w(y) = -\infty,$$

which indecates that this model is indeed insufficient.

In order to correct this problem, a German named Ludwig Prandtl and several of his collegues replaced the horseshoe vortex with a vortex sheet [2]—in other words, a continuous distribution of horseshoe vortices [Figure 12]. In this model, the differential cirrculation at a point is equal to the summation of all the differential filaments from the closest tip to that point. Using this model, we can express a differential downwash element at some position y_0 as

$$dw(y_0) = -\frac{d\Gamma}{4\pi(y_0 - y)} = -\frac{d\Gamma/dy}{4\pi(y_0 - y)}\, dy. \tag{6}$$

Thus, the downwash at any point y_0 is given as

$$w(y_0) = -\frac{1}{4\pi} \int_{-b/2}^{b/2} \frac{d\Gamma/dy}{y_0 - y}\, dy. \tag{7}$$

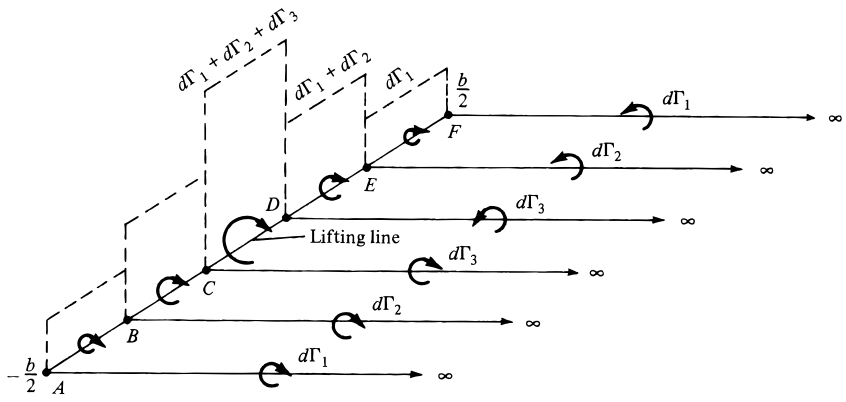

Figure 12: Differential $\Gamma(y)$ distribution along a wing [2].

Now that the amount of downwash can be quantified, one can find the induced angle of attack α_i quite easily. Observing Figure 8,

$$\alpha_i(y_0) = \arctan\left(-\frac{w(y_0)}{V_\infty}\right) \approx -\frac{w(y_0)}{V_\infty}, \tag{8}$$

assuming α_i is small. Substituting Eq.7 into Eq.8,

$$\alpha_i(y_0) = \frac{1}{4\pi V_\infty}\int_{-b/2}^{b/2} \frac{d\Gamma/dy}{y_0 - y}\, dy. \tag{9}$$

Since $\alpha_{\text{eff}}(y_0) = \alpha - \alpha_i(y_0)$, the lift coefficient $c_l(\alpha_{\text{eff}})$ can be found assuming the c_l distribution for the particular airfoil section at y_0 is known. Thus, the total lift for the wing can be found:

$$L'(y_0) = \frac{1}{2}\rho_\infty V_\infty^2 c(y_0) c_l(\alpha_{\text{eff}}), \tag{10}$$

$$L = \int_{-b/2}^{b/2} L'(y)\, dy. \tag{11}$$

2.2 Numerical Model & Implementation

Because the distribution of $\Gamma(y)$ is unknown, the process of solving for lift presents non-linearities; thus, these values must be solved for using numerical techniques. The following sections describe in detail the mathematical and numerical models used in finding the required values of the blade, such as lift and required rpm, and what the optimal geometry of the rotor blade is after performing a numerical analysis from these models.

2.2.1 Mathematical Model

In order to model one of the rotor blades mathematically, let us picture the blade as a finite wing. However, when comparing a wing from a fixed-wing aircraft to a helicopter blade,

one notices a fundamental difference: the freestream velocity distribution varies with rotor position for a helicopter, while V_∞ is uniform for a fixed-wing aircraft. Though this small difference may seem trivial, it presents singularities at the end of the blade near the rotor hub. From the equation describing the induced angle of attack [Eq.8], if r represents the direction originating at the axis of rotation and extending outward along the blade,

$$\lim_{r\to 0} \alpha_i(r) = -\infty, \tag{12}$$

which presents severe problems in the model.

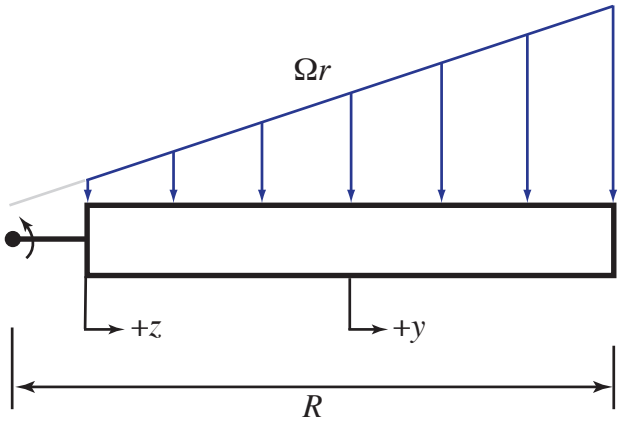

Figure 13: Diagram depicting the rotor blade model under consideration.

Thus, let us describe the rotor blade as in Figure 13, where a blade section is spinning from an infinitely thin wire. In this model, the length of both the wire and the blade make up the distance R, the blade length is b, and the wire is some small fraction x of R. Accordingly, the length of the blade section $b = (1-x)R$. In addition, the blade section is subjected to a freestream velocity Ωr, which in terms of the y-axis that originates at the center of the blade section is

$$U(y) = \frac{\Omega}{2}\left(R + Rx + 2y\right). \tag{13}$$

Now, let us define several expressions that will aid us in optimizing the rotor blade geometry. According to Bramwell [4], the thrust coefficient for a helicopter blade is

$$t_c \equiv \frac{T}{\rho s A \Omega^2 R^2} = \frac{1}{2}\int_0^1 (z^*)^2 c_l \; dz^*, \tag{14}$$

where T is the thrust, ρ is the air density, and A is the rotor disc area. The rotor solidity is $s \equiv nc/\pi R$, where n is the number of rotor blades and c is the chord length. The dimensionless variable z^* is analogous to the z-axis as before, only $z^* \equiv z/b,\ z^* \in [0,1]$.

Similar to the thrust coefficient, the torque coefficient is defined as follows:

$$q_c \equiv \frac{Q}{n\rho c \Omega^2 R^4} = \frac{\delta}{8} + \frac{1}{2}\int_0^1 (z^*)^3 \alpha_i c_l \; dz^*. \tag{15}$$

The value δ can be estimated from Bramwell [4]:

$$\delta \approx 0.0087 - 0.0216\alpha_{\text{eff}} + 0.4\alpha_{\text{eff}}^2, \tag{16}$$

where α_{eff} is expressed in radians. Using the following definitions, we are able to provide another parameter called the figure of merit

$$M = \frac{t_c^{3/2}}{q_c}\sqrt{\frac{s}{2}}, \tag{17}$$

which is a dimensionless value that indicates the overall "performance" of a particular rotor blade geometry [4].

Though the equations just presented may seem arbitrary, they help provide a clear measure of how different blade geometries compare in terms of performance. In general, an ideal geometry is one that maximizes the thrust coefficient, minimizes the torque coefficient, and maximizes the figure of merit. The torque coefficient must be as high as possible, since a larger t_c results in a smaller required rpm for hover from the equation

$$\hat{\Omega} = \sqrt{\frac{900W}{\rho s \pi^3 R^4 t_c}}, \tag{18}$$

where $\hat{\Omega}$ is the required rotational speed for hover, and W is the weight of the MAV. Equivalently, the torque coefficient q_c must be minimized in order to reduce the required power for flight. As a result, a maximized t_c and a minimized q_c result in a maximized M [Eq.17].

2.2.2 Numerical Implementation of the Lifting-Line Method

As mentioned previously, Prandtl's lifting-line theory cannot be used directly as the process of finding $\Gamma(y)$ is nonlinear. Thus, a numerical model must be created [6]. The first step is to choose a number N large such that $N \in \mathbb{N}$ and $N \bmod 2 = 0$ (*ie.* 150, 200, etc.). In this way, the rotor blade section will be discretized into $N+1$ equally spaced nodes [Figure 14]. Odd nodes are denoted by a filled circle, while even nodes are denoted by an open circle. The nodes are "staggered" in order to avoid numerical complications; $\Gamma(y_j)$ and $\alpha_i(y_j)$ will be computed on the odd nodes, while the integrals in $\alpha_i(y_j)$ [Eq.9] will be calculated along the even nodes.

Because $\Gamma(y)$ is unknown, a guess must be supplied for each $\Gamma(y_j)$ at the odd nodes. A reasonable initial guess would be an elliptic distribution [2]; thus, a value for Γ_0 is chosen such that

$$\Gamma(y_j) = \Gamma_0\sqrt{1 - \left(\frac{y_j}{b/2}\right)^2}.$$

The values of $\alpha_i(y_j)$ must be calculated on each of the odd nodes as well; however, in order to avoid singularities at the end nodes, the required integrands will be computed on the even nodes. Converting these integrals into finite sums using Simpson's 1/3 rule:

$$\int_{y_2}^{y_N} \frac{d\Gamma/dy}{y_j - y}\, dy \approx \Delta y \left(\frac{(d\Gamma/dy)_2}{y_j - y_2} + \frac{(d\Gamma/dy)_N}{y_j - y_N} + 2\sum_{k=4}^{N-2} \frac{(d\Gamma/dy)_k}{y_j - y_k} \right), \quad k \text{ even.} \tag{19}$$

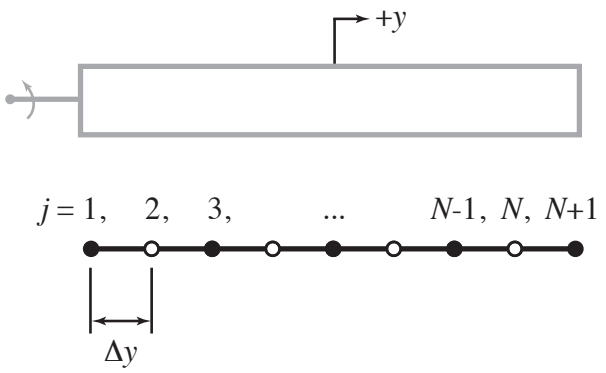

Figure 14: Numerical model of the rotor blade.

Additionally, $(d\Gamma/dy)_k$ can be approximated using the following:

$$\left(\frac{d\Gamma}{dy}\right)_k \approx \frac{\Gamma_{k+1} - \Gamma_{k-1}}{2\Delta y}. \tag{20}$$

For brevity, we will introduce the notation

$$F_i \equiv \frac{(d\Gamma/dy)_i}{y_j - y_i}, \quad i = \{1, 2, \ldots, N+1\}.$$

Though Eq.19 gives us a good estimation of the integral expressed in Eq.9, it does not account for the contributions at each end of the rotor blade. These integrands at the first and last intervals can be estimated by

$$\int_{y_1}^{y_2} \frac{d\Gamma/dy}{y_j - y}\, dy \approx \frac{\Delta y}{2}\left(F_1 + F_2\right), \tag{21}$$

$$\int_{y_N}^{y_{N+1}} \frac{d\Gamma/dy}{y_j - y}\, dy \approx \frac{\Delta y}{2}\left(F_N + F_{N+1}\right). \tag{22}$$

Of course, both F_1 and F_{N+1} are unknown values, but they can both be approximated by extrapolation using a first-order Taylor series expansion:

$$F_1 \approx \frac{3F_2 - F_4}{2},$$

$$F_{N+1} \approx \frac{3F_N - F_{N-2}}{2}.$$

Thus, the contributions from Eq.21 and Eq.22 can be summed with the result from Eq.19 to form the entire integral in Eq.9.

Once $\alpha_i(y_j)$ is found for the each odd node, $\alpha_{\text{eff}}(y_j)$ can also be calculated from $\alpha_{\text{eff}}(y_j) = \alpha(y_j) - \alpha_i(y_j)$. Knowing $\alpha_{\text{eff}}(y_j)$, the values $c_l(y_j)$ can be found from airfoil data. For this application, coordinate data for various airfoils were taken and imported into the open-source potential flow solver *XFOIL*[4] using a custom *MATLAB* program [Appendix A.1]. Figure 15 is an example of the resulting output once a custom airfoil is imported into *XFOIL*.

[4] *XFOIL*: Subsonic Airfoil Development System. `http://web.mit.edu/drela/Public/web/xfoil/`

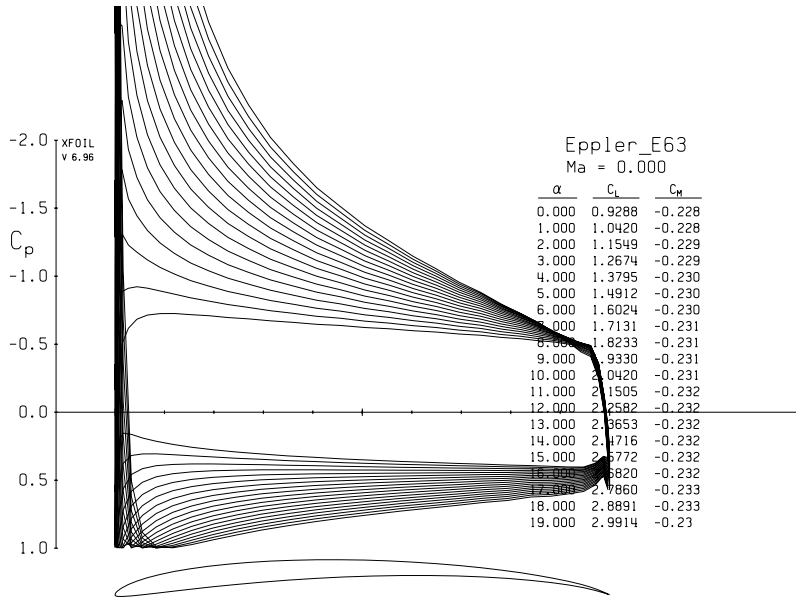

Figure 15: *XFOIL* output for a particular airfoil.

At this point, a new circulation distribution can be calculated:

$$\Gamma'_j = \frac{1}{2}U(y_j)c(y_j)c_l(y_j), \quad j \text{ odd.} \tag{23}$$

Using Γ'_j, convergence can be checked by taking $d_j = \left|\Gamma'_j - \Gamma_j\right|$ for each j and then finding $||\mathbf{d}||$. If not yet converged, then the circulation distribution must be updated using the equation

$$\Gamma_j = \Gamma_j + D(\Gamma'_j - \Gamma_j), \tag{24}$$

where D is a convergence damping parameter approximately equal to 0.035. Of course, for proper convergence, each iteration must impose $\Gamma_1 = \Gamma_{N+1} = 0$.

Once $\mathbf{\Gamma}$ has converged, the following values from Section 2.2.1 can be approximated using Simpson's 1/3 rule along the odd nodes:

$$t_c \approx \frac{\Delta z^*}{2}\sum_{j=3}^{N-1}\left(\frac{z_j}{b}\right)^2 c_l(y_j), \tag{25}$$

$$\delta_{\text{avg}} \approx 2\Delta z^*\sum_{j=3}^{N-1}\left(0.0087 - 0.0216\alpha_{\text{eff}}(y_j) + 0.4\alpha_{\text{eff}}(y_j)^2\right), \tag{26}$$

$$q_c \approx \frac{\delta_{\text{avg}}}{8} + \Delta z^*\sum_{j=3}^{N-1}\left(\frac{z_j}{b}\right)^3 \alpha_i(y_j)c_l(y_j), \tag{27}$$

where $\Delta z^* = \Delta y/b$. Using these values, M and $\hat{\Omega}$ can be found simply from Eq.17 and Eq.18. Please note, however, that results from this method can be assumed accurate only within 20% [2].

2.2.3 Numerical Implementation Results

By comparing the values of $\hat{\Omega}$, q_c, and M, an optimal blade geometry can be found theoretically. However, the numerical analysis must be first be verified through testing. Once the analysis algorithm had been written in *MATLAB* [Appendix A.2], the rotor blade from an E-flite CX2 R/C helicopter [5] was taken and modeled in the program, including length, taper ratio, and airfoil profile. By hanging small weights from the CX2 and recording its rotor speed at hover for each weight value, the distribution of t_c vs. rpm was found by marking a rotor blade tip and reading the blade speed using a handheld tachometer [Figure 16].

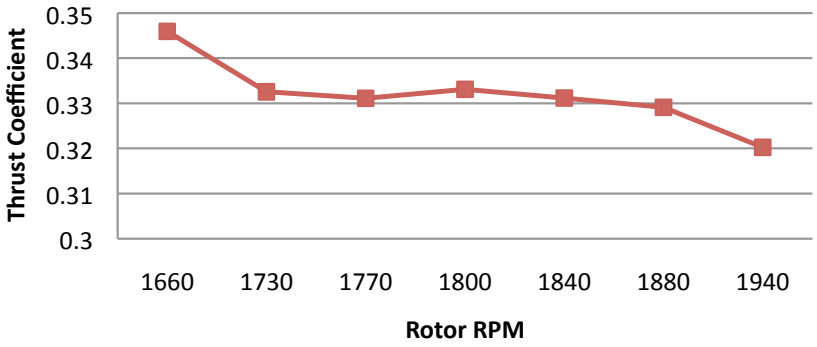

Figure 16: Experimental variation of $t_c(\hat{\Omega})$ for the E-flite CX2.

Computing the mean t_c for the test data resulted in a value of 0.332. However, regardless of the rpm, the *MATLAB* software returned a value of 0.197 for each case. This result makes sense: the parameter $t_c = t_c(\text{geometry})$, so the speed of the rotor blades would not affect this value. Nevertheless, how do we account for this difference between the test data and the theoretical data? For this application, errors within the model—including the fact that the test helicopter has two sets of rotor blades while the model only takes one into account—is assumed to be encompassed by one dimensionless thrust coefficient correction factor

$$B = \frac{t_c}{t_c)_{\text{model}}} = \frac{0.332}{0.197} \approx 1.7, \tag{28}$$

which is used to correct the value of t_c. Because verifying an experimental q_c would prove difficult, we assume that the value produced by our software is correct; however, we also recognize that it may not necessarily be reliable.

Now that t_c has been adjusted through experimentation, $\hat{\Omega}(t_c)$ is taken to be correct; moreover, the blade analysis may be continued. The first geometrical aspect under evaluation is the airfoil profile. In order to compare different airfoils, several airfoil profiles with their corresponding $c_l(\alpha)$ data are taken and imported into our custom *MATLAB* program. The results can be seen in Figure 17.

Observing Figure 17, the Althaus AH 7-476 airfoil profile is quite desirable since $\hat{\Omega}$ is minimized. However, we find that this airfoil performs somewhat poorly when comparing the figure of merit M, which must be maximized. In this case, which airfoil is best? Since

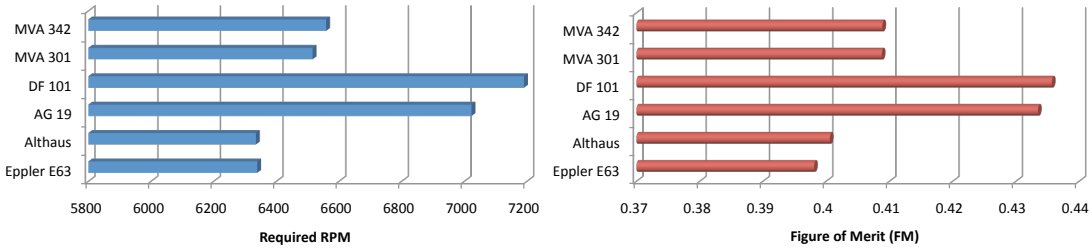

(a) Airfoil section vs. required blade rpm. (b) Airfoil section vs. figure of merit.

Figure 17: Resulting (a) $\hat{\Omega}$(airfoil) and (b) M(airfoil).

$M = M(t_c, q_c)$ and q_c has an unknown reliability, M cannot be regarded as more important than $\hat{\Omega}$, which is only a function of t_c. Furthermore, since these optimizations are made merely to reduce the required load on the MAV power system during flight, the parameter $\hat{\Omega}$ is very important given that the power consumption in brushless DC motors is a strong function of their rotational speed. Also, it is worth noting that as the amount of lift that a wing produces increases, the induced drag increases as well, thus increasing q_c and lowering M. As a result, rotor blades that produce more lift for a given rotational speed will possess a lower figure of merit; hence, the Althaus AH 7-476 is considered to be the ideal airfoil.

The next geometrical aspect of the blade that will be studied is the taper ratio $a = c_t/c_r$, where c_r is the chord at the root of the rotor blade and c_t is the chord at the tip of the rotor blade. For simplicity of analysis and manufacturing, this evaluation will only consider linear taper ratios. Consequently, we desire to produce a linear chord profile in our software using only the parameters c_{avg} and a; thus, taking the two equations that describe the taper of the blade and solving, we obtain

$$\mathbf{c} = \begin{bmatrix} 0.5 & 0.5 \\ a & -1 \end{bmatrix}^{-1} \begin{pmatrix} c_{\text{avg}} \\ 0 \end{pmatrix} = \frac{2c_{\text{avg}}}{1+a} \begin{pmatrix} 1 \\ a \end{pmatrix}, \tag{29}$$

where $\mathbf{c}(1,1) = c_r$ and $\mathbf{c}(2,1) = c_t$. Placing these two parameters into the equation

$$c_j = \frac{1}{R}(Rc_r - z_j c_r + z_j c_t), \tag{30}$$

the chord length for each j-th node can be obtained.

By varying the taper ratio a from 0.3 to 1.0, the data we acquired from the analysis using a value of $N = 180$ and $c_{\text{avg}} = 20$ mm can be found in Figure 18a. Again, since $\hat{\Omega}$ must be minimized while M must be maximized, an ideal taper ratio of $a = 0.3$ is the obvious choice. Though both of these parameters seem to diverge as a becomes small, a minimum is soon reached for $\hat{\Omega}$ for $a < 0.3$, rendering a taper ratio any smaller than 0.3 impractical [4]. Thus, $a = 0.3$ is the ideal taper ratio.

Next, an ideal rotor blade twist can be calculated using the same numerical tool as before. At the root, a geometric angle of attack (pitch) of 18° is taken at the blade root, since it is very close to $c_{l,\max}$ for the Althaus AH 7-476 airfoil. However, there exists an unknown $\Delta\alpha$ from the root to the tip of the blade. Again, for sake of simplicity, a linear twist profile

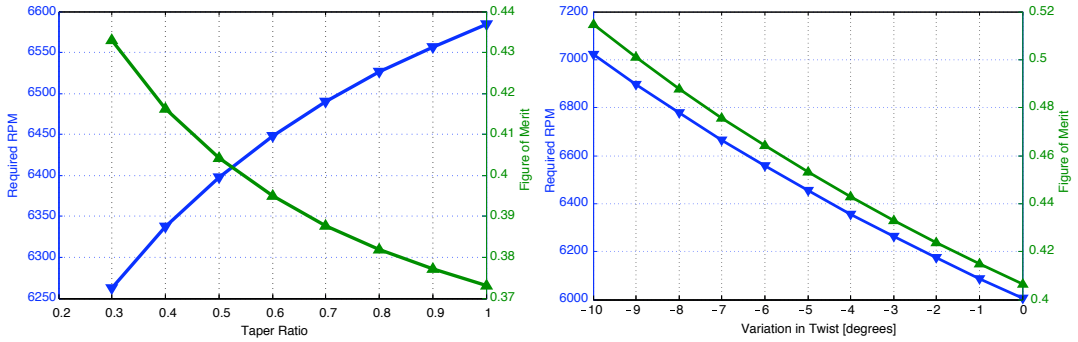

(a) $\hat{\Omega}$ and M vs. taper ratio a. (b) $\hat{\Omega}$ and M vs. variation in twist $\Delta\alpha$.

Figure 18: Numerical results from *MATLAB*.

is assumed along the rotor blade. By choosing $\Delta\alpha$, one can create a pitch profile along the computational cells through the equation

$$\alpha_j = \Delta\alpha z_j^* + \alpha_0, \tag{31}$$

where $\alpha_0 = 18°$ is the initial pitch at the root. After finding α_j, the effective angle of attack can again be found easily using $\alpha_{\text{eff}}(y_j) = \alpha_j - \alpha_i(y_j)$. Figure 18b gives the relation between $\hat{\Omega}$, M, and $\Delta\alpha$.

Figure 18b presents a similar conundrum as compared to the airfoil profile analysis: minimizing $\hat{\Omega}$ results in a decreasing M, while an increasing $\hat{\Omega}$ results in maximizing M. As before, the optimization of $\hat{\Omega}$ takes prominence over the optimization of M; thus, the variation of twist $\Delta\alpha$ is taken to be $-3°$. In order to qualitatively verify the results obtained, the lift per unit span of the rotor blade L' is plotted versus the blade location and compared against a figure portraying typical rotor blade loading from a common helicopter aerodynamics textbook [9], as seen in Figure 19. As one may notice, the profiles look very similar, which asserts that this numerical analysis may be valid.

In summary, the following list specifies the optimal geometric properties of the MAV's rotor blades:

- Length $R^\star$: **80 mm**
- Airfoil profile: **Althaus 7-476**
- Average chord length $c^\star_{\text{avg}}$: **20 mm**
- Taper ratio a: **0.3**
- Twist (pitch) variation $\Delta\alpha$: $\mathbf{-3}°$ $\quad(18° \rightarrow 15°)$

where $\star$ denotes those geometrical parameters that were chosen, not optimized. The final CAD rendering of a set of optimized rotor blades, including the swash plate assembly, is displayed in Figure 20.

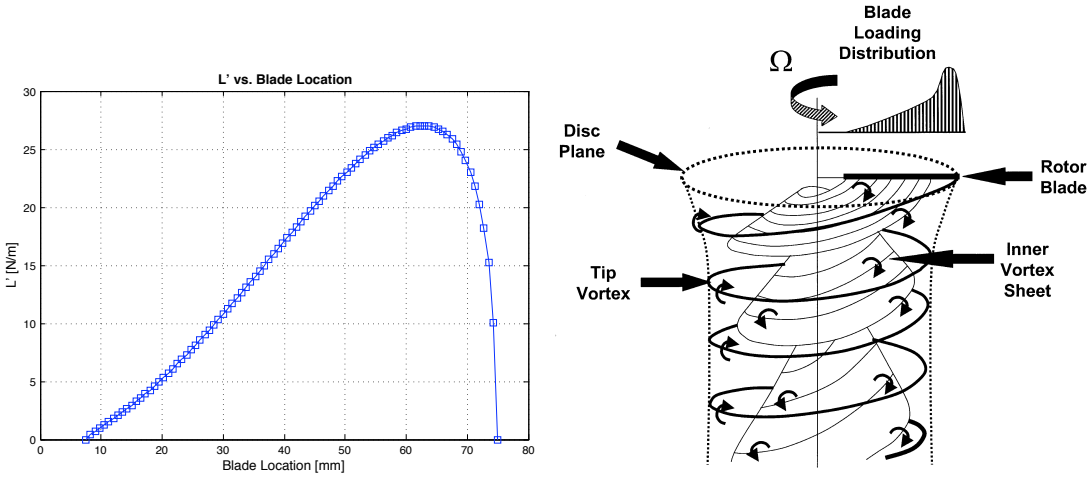

(a) (b)

Figure 19: Blade loading distribution from (a) the numerical analysis and from (b) Seddon and Newman's *Basic Helicopter Aerodynamics* [9].

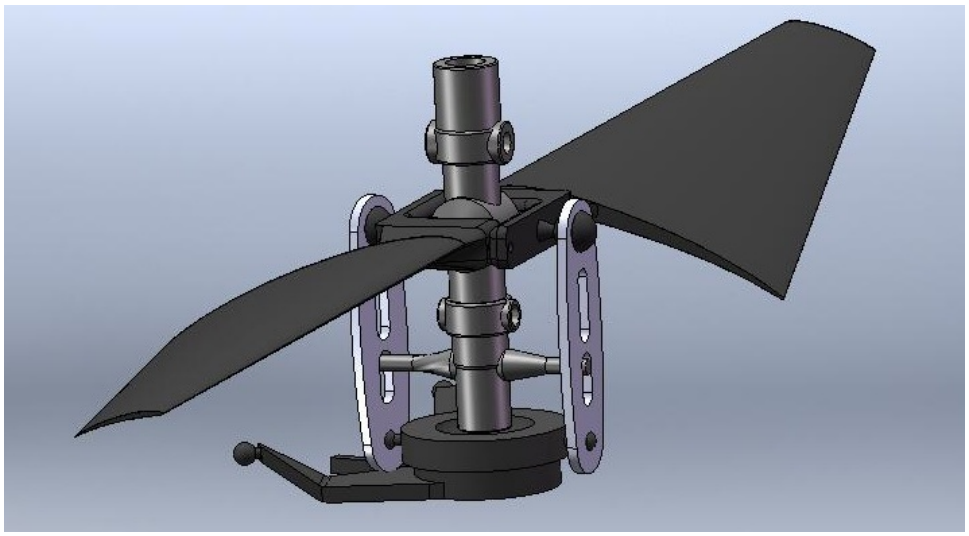

Figure 20: CAD rendering of optimized rotor blades with swash plate assembly.

3 Conclusion

Micro air vehicles have the potential to be effectively implemented in situations where information must be obtained with minimal loss of life and property. Optimization of the coaxial rotor blades has played an integral role in this MAV design, given that the rotor blades are one of the few components able to be optimized. Through the numerical implementation of proven aerodynamic concepts such as Prandtl's lifting-line theory, the analysis in this paper was able to reveal the particular blade parameters (*ie.* taper and twist) that maximize the overall lift obtained by the MAV for a given rotor blade speed. The numerical routines were performed using *MATLAB*, and the results indicated that the ideal rotor blade geometry would possess the Althaus 7-476 airfoil profile, a length of 80 mm, an average chord length of 20 mm, a taper ratio of 0.3, and a twist variation of -3°.

Acknowledgments

This project has been made possible by the whole-hearted support of many individuals. I would like to thank the Louisiana Space Consortium, LaSPACE, and Dr. John Wefel, director of LaSPACE, for the financial support for this project. I am also grateful to our project advisor, Dr. Shengmin Guo, and our senior design class instructor, Dr. Muhammad Wahab, both from the LSU Mechanical Engineering Department, for their continued guidance and support. I would like to thank Dr. Keith Gonthier for his aerodynamics class which helped our MAV team delve into the complexities present within the aerodynamic analysis. I would also like to thank Edward Scheuermann, LSU Mechanical Engineering Junior, for valuable advice and help with the manufacturing and testing procedures. Most importantly, I would like to thank the other members of the MAV team: Diane Ho, Lauren Peltier, and Richie Sajan; their support, encouragements, and contributions have been critical to the success of this project. Without them, this paper would not be possible.

References

[1] 7th European Micro Air Vehicle Conference and Flight Competition. `http://www.mav07.org`, 2007.

[2] Anderson, John D. *Fundamentals of Aerodynamics*. McGraw-Hill, fourth edition, 2007.

[3] Bohorquez, F. and Pines, D. Hover performance and swashplate design of a coaxial rotary wing micro air vehicle. *Annual forum proceedings*, 1:629–641, 2004.

[4] Bramwell, A.R.S. *Helicopter Dynamics*. Butterworth-Heinemann Ltd, 1976.

[5] E-flite CX2 Coaxial Micro Helicopter. `http://www.e-fliterc.com/Products/Default.aspx?ProdID=EFLH1250`.

[6] Gonthier, Keith A. Numerical Implementation of a Lifting-Line Method. ME 4943 Class Handout, Fall 2007.

[7] Halliday, D., Resnick, R., and Walker, J. *Fundamentals of Physics*. Wiley, seventh edition, 2004.

[8] McMichael, J.M. and Col. Francis, M.S. Micro Air Vehicles – Toward a New Dimension in Flight. Technical report, `http://www.fas.org/irp/program/collect/docs/mav_auvsi.htm`, August 1997.

[9] Seddon, J. and Newman, S. *Basic Helicopter Aerodynamics*. Blackwell Science Ltd, second edition, 2002.

[10] Swash plate diagram. `http://www.delftoutlook.tudelft.nl/info/images/031003122258110.jpg`.

[11] US Navy MAV. `http://en.wikipedia.org/wiki/Image:MicroAirVehicle.jpg`.

Appendices

A MATLAB Code

A.1 Airfoil Data Conversion for *XFOIL*

```
% airfoil_convert.m - Convert airfoil data from Profili database
%                      into an XFOIL compatible format.
% ME 4243
% Written by Jeff Kornuta

% set some parameters
clear airfoil;  % clearn out old variable
L1 = 17;        % number of points on upper surface
L2 = 17;        % number of points on lower surface

% switch up top coordinates and reduce by factor of 100
% for points on upper surface
n = L1;
for i = 1:L1
    airfoil(i,1) = temp(n,1)*1e-2;
    airfoil(i,2) = temp(n,2)*1e-2;
    n = n-1;
end;

% just reduce by factor of 100 for points on lower surface
for i = (1+L1):(L1+L2)
    airfoil(i,1) = temp(i,1)*1e-2;
    airfoil(i,2) = temp(i,2)*1e-2;
end;

% export data to .dat file for XFOIL
newfile = fopen('./althaus.dat','wt');

% print first line to specify airfoil name
fprintf(newfile,'Althaus\n');

% now print all data nice & neat
for j = 1:(L1+L2)
    fprintf(newfile,'%.6f %.6f',airfoil(j,1),airfoil(j,2));
    if (j ~= (L1+L2))
        fprintf(newfile,'\n');
    end;
end;

% voila!
fclose(newfile);
```

A.2 Main Analysis Program

```
% program.m   -          Main program for numerical analysis of
%                        the rotor blades
% ME 4243
% Written by Jeff Kornuta

clear all;
for m = 1:1

    % a = .3:.1:1;
    a(m) = .3;
    cavg = .02;
    C = inv([.5 .5; a(m) -1])*[cavg; 0];
%clc;

% define some preliminary constants
R = .075;
%A = pi*R^2;
x = .1;
b = (1-x)*R;
%AR = 6;
rpm = 6300;
omega = pi*rpm/30;
rho = 1.225;
%c = b/AR
%S = b*c;
%S = 2749.9e-6;
%cavg = S/R;
s = 2*cavg/(pi*R);
%s = 2*cavg(m)/(pi*R);
%s = 2*S/(pi*R^2);
%AR = b^2/S;
alpha0 = 18*(pi/180);
N = 180;
gamma0 = 50;
D = .035;
dy = b/N;
iterations = 0;
diff = ones(1,N+1);

% load up some variables -- it's fun!
i = 1;
for j = 1:(N+1)
    y(j) = -(b/2)+(j-1)*dy;
    U(j) = pi*rpm/60*(R+R*x+2*y(j));
    z(j) = (j-1)*dy;

```

```
47      % twist, anyone?
48      alpha(j) = -3*pi/180*(z(j)/b)+alpha0;
49
50      % even dynamic taper!
51      c(j) = (C(1)*R-C(1)*z(j)+C(2)*z(j))/R;
52
53      % make odd gammas and specify an odd y for plotting
54      if (mod(j,2) == 1)
55          gamma(j) = gamma0*sqrt(1-(2*y(j)/b)^2);
56          Y(i) = y(j);
57          BigU(i) = U(j);
58          Z(i) = z(j);
59          i = i+1;
60      end;
61  end;
62
63  % set dz
64  dx = (z(2)-z(1))/b;
65
66  % start convergence loop
67  while (norm(diff) > 1e-5)
68      i = 1;
69      iterations = iterations+1;
70      diff = zeros(1,N+1);
71
72      for j = 1:2:(N+1)
73          gammaold(j) = gamma(j);
74
75          % find dGamma/dy over even nodes
76          for k = 2:2:N
77              dgdy(k) = (gamma(k+1)-gamma(k-1))/(2*dy);
78              F(k) = dgdy(k)/(y(j)-y(k));
79          end;
80
81          % sum up integrals over even nodes
82          sumk(j) = F(2)+F(N)+2*sum(F(4:(N-2)));
83          sumk(j) = dy*sumk(j)+.5*dy*(.5*(3*F(2)-F(4))+F(2)+...
84                                      F(N)+.5*(3*F(N)-F(N-2)));
85
86          % find alpha values
87          alphai(j) = sumk(j)/(4*pi*U(j));
88          alphaeff(j) = (alpha(j)-alphai(j))*(180/pi);
89
90          % find cl using specific airfoil data (NACA 0009)
91          % if (alphaeff(j) <= 13)
92          %    cl(j) = .1038*alphaeff(j);
93          %else
```

```
94          %    cl(j) = -.06667*alphaeff(j)+2.217;
95          %end;
96
97          % find cl using XFOIL airfoil data (Eppler E49)
98          %cl(j) = -.00171*alphaeff(j)^2+.1124*alphaeff(j)+1.302;
99          %cl(j) = .104*alphaeff(j)+1.307;
100
101         % XFOIL airfoil data for Eppler E63
102         %cl(j) = .11*alphaeff(j)+.9376;
103
104         % Airfoil data for Althaus
105         cl(j) = .1129*alphaeff(j)+.9172;
106
107         % Airfoil data for AG 19
108         %cl(j) = .1326*alphaeff(j)+.259;
109
110         % Airfoil data for DF 101
111         %cl(j) = .1184*alphaeff(j)+.2647;
112
113         % Airfoil data for MVA 301
114         %cl(j) = .1159*alphaeff(j)+.7499;
115
116         % Airfoil data for MVA 342
117         %cl(j) = .1107*alphaeff(j)+.7524;
118
119         % compute new gamma
120         gammanew(j) = .5*U(j)*c(j)*cl(j);
121
122         % "finish him!"
123         if (j~=1 && j~=(N+1))
124             gamma(j) = gammaold(j)+D*(gammanew(j)-gammaold(j));
125             diff(j) = abs(gamma(j)-gammaold(j));
126         else
127             gamma(j) = 0;
128         end;
129
130         % make life easier down the road
131         gammasin(j) = gamma(j)*sin(alphai(j));
132         tsum(j) = (z(j)/b)^2*cl(j);
133         delta(j) = .0087-.0216*(pi/180*alphaeff(j))+...
134                                 .4*(pi/180*alphaeff(j))^2;
135         qsum(j) = (z(j)/b)^3*alphai(j)*cl(j);
136         lp(j) = rho*U(j)*gamma(j);
137         %csum(j) = (z(j)/b)^2*c(j);
138
139         % make semi-pretty matrices to plot
140         Alphai(i,m) = alphai(j)*(180/pi);
```

```
141         Alphaeff(i,m) = alphaeff(j);
142         Gamma(i,m) = gamma(j);
143         Cl(i,m) = cl(j);
144         Delta(i,m) = delta(j);
145         Lp(i,m) = lp(j);
146         i = i+1;
147
148     end;
149
150     % damage control for endpoints
151     Alphai(1,m) = Alphai(2,m)+Alphai(3,m)-Alphai(4,m);
152     Alphaeff(1,m) = Alphaeff(2,m)+Alphaeff(3,m)-Alphaeff(4,m);
153     Alphai(N/2+1,m) = Alphai(N/2,m)+Alphai(N/2-1,m)-Alphai(N/2-2,m);
154     Alphaeff(N/2+1,m) = Alphaeff(N/2,m)+Alphaeff(N/2-1,m)-Alphaeff(N/2-2,m);
155     Cl(1,m) = 0;
156     Cl(N/2+1,m) = 0;
157     Lp(1,m) = 0;
158     Lp(N/2+1,m) = 0;
159
160 end;
161
162 % get thrust coefficient & others
163 deltaavg(m) = 2*dy/b*sum(delta(3:N-1));
164 %T = rho*cavg*omega^2*R^3*dx*sum(tsum(3:N-1));
165 tc(m) = .5*dx*sum(tsum(3:N-1))
166 qc(m) = deltaavg(m)/8+dx*sum(qsum(3:N-1))
167 RPM(m) = sqrt(900*(205*9.807e-3)/(rho*s*pi^3*R^4*(1.7*tc(m))));
168 %Q(m) = qc(m)*rho*s*pi*omega^2*R^5;
169 Q(m) = deltaavg(m)*rho*2*cavg*omega^2*R^4/8+...
170 .5*rho*2*cavg*omega^2*R^4*sum(qsum(3:N-1))
171 %tcopt = .5*(deltaavg/sqrt(s))^(2/3);
172 M(m) = sqrt(s/2)*tc(m)^1.5/qc(m);
173 %Mt = tc/tcopt
174
175 end;
```